41st Aerospace Sciences Meeting and Exhibit
6-9 January 2003, Reno, Nevada

AIAA 2003-1271

Effects of RANS Turbulence Modeling on Calculation of Lobed Nozzle Flowfields

Nicholas J. Georgiadis *
NASA Glenn Research Center, Cleveland, OH 44135

Christopher L. Rumsey †
NASA Langley Research Center, Hampton, VA 23681

Dennis A. Yoder ‡and Khairul B.M.Q. Zaman §
NASA Glenn Research Center, Cleveland, OH 44135

Two Reynolds-averaged Navier-Stokes solvers, CFL3D and WIND, are applied to the subsonic turbulent jet flowfield originating from a six-lobed nozzle, with emphasis placed on turbulence modeling effects. The turbulence models investigated included linear one-equation and two-equation models and nonlinear two-equation explicit algebraic stress model (EASM) formulations. Two nozzle operating points are investigated, corresponding to exit Mach numbers of 0.30 and 0.94. The one-equation model solutions provided reasonable agreement with experimentally measured velocities, but not with turbulence intensities. The linear two-equation model calculations resulted in delayed initial mixing rates but reasonable agreement with data further downstream. Calculations obtained with a modified $K-\omega$ EASM provided reasonable agreement with mean velocity data and were in the best agreement with data for turbulence intensities. The Mach 0.30 $K-\omega$ EASM calculation exhibited an unsteadiness in the initial jet region, which is believed to be characteristic of the nozzle flow under consideration.

Introduction

Computational fluid dynamics (CFD) codes have become an attractive option for the analysis of aerospace systems due to advances in flow solver and computer hardware technologies. For the investigation of one particular class of flows, that of aircraft engine exhaust nozzles, Reynolds-averaged Navier-Stokes (RANS) solvers have been used extensively in recent years. In the RANS approach, all effects of turbulence are replaced with a turbulence model. However, with realistic nozzle flows typically dominated by turbulent mixing, the accuracy of a flow simulation is usually determined by the capabilities of the turbulence model employed. Previous studies, such as those of Barber et. al[1] and Georgiadis et. al,[2] investigated linear two-equation turbulence models for calculation of benchmark nozzle and mixing layer test cases, and determined that such models have difficulty predicting the effects of compressibility, high temperatures, and three dimensional flow features.

To further address the complexities of three dimensional nozzle flowfield development, a nozzle having a six-lobed configuration is investigated in the current work. Although this nozzle is more geometrically complex than those investigated in the studies of Refs. 1 and 2, the nozzle was tested using unheated air and had a subsonic exit condition. As a result, temperature and compressibility effects are not significant factors, and the effects of three-dimensional flow could be isolated. Two general purpose RANS solvers, CFL3D and WIND, are used to obtain calculations for this lobed nozzle configuration. Linear one-equation and two-equation turbulence models, such as those employed in Refs. 1 and 2, are used here. In addition, more sophisticated nonlinear explicit algebraic stress model (EASM) formulations are also investigated.

Experimental Configuration

In the experiments of Zaman and Wang,[3] the free jets developing from a circular nozzle and three lobed nozzles, having six, ten, and fourteen lobes respectively, were investigated. These lobed nozzle configurations exhibited lower turbulence intensities and lower far field noise than non-lobed configurations. The six-lobed configuration, shown schematically in Fig. 1, is under investigation in the current work. All of the nozzles investigated in Ref. 3 had convergent interiors with a 0.25 inch long constant area cross-section just upstream of the nozzle exit plane. In addition, the equivalent diameter, D, based on an area-equivalent round nozzle, was 0.58 in. for all of the nozzles. In the experiments, hot-wire anemometry was used to make

*Aerospace Engineer, Nozzle Branch, Senior Member AIAA
†Aerospace Engineer, Computational Modeling and Simulation Branch, Associate Fellow AIAA
‡Aerospace Engineer, Nozzle Branch, Member AIAA
§Aerospace Engineer, Nozzle Branch, Associate Fellow AIAA

measurements of mean flow axial velocity and turbulence intensity fields for Mach 0.30 and Mach 0.94 nozzle exit operating points. As discussed in Ref. 3, using the hot-wire technique in high speed flows, as in the case of the Mach 0.94 nozzle flow considered here, has limitations. As a result, measurements were only taken along the jet centerline for the Mach 0.94 case. For the Mach 0.30 case, measurements were not only made along the centerline, but also detailed velocity and turbulence intensity profiles were obtained along the jet major and minor axes at several axial stations.

Computational Modeling

Two widely used RANS solvers are employed to conduct the computational investigations of the six-lobed nozzle in this work. The first is WIND,[4] the production flow solver of the NPARC Alliance, a joint code development group of NASA Glenn Research Center, USAF Arnold Engineering Development Center, and the Boeing Company. The second is CFL3D,[5] a flow solver developed at NASA Langley Research Center. Both WIND and CFL3D are structured-grid finite volume codes using upwind numerical schemes for most flow applications, and in the current study, the flux difference-splitting technique of Roe was employed to calculate fluxes at cell faces. Both WIND and CFL3D can accommodate point-matched, patched, or overset grids for complex computational domains, and can employ local time-step scaling and grid-sequencing to accelerate convergence for steady state problems. CFL3D also has a multigrid capability for convergence acceleration. Grid sequencing in both WIND and CFL3D was used for the calculations obtained in the current study.

Turbulence Modeling

Both CFL3D and WIND have a broad set of turbulence models available, all of which fall into the class of eddy-viscosity formulations. In the current study, a subset of these models was chosen to investigate the effects of model formulations and sophistication, i.e. linear one-equation, linear two-equation, and nonlinear two-equation EASM approaches. In the cases of the same model from this subset being available in both CFL3D and WIND, solutions with both codes were obtained to isolate differences due to code.

The linear one-equation model investigated with both solvers is the Spalart-Allmaras[6,7] (SA) formulation. The SA model is available in both CFL3D and WIND. The linear two-equation turbulence models investigated here are the Chien $K-\epsilon$[8] model and the shear-stress transport (SST) model of Menter.[9,10] The SST model employs a $K-\omega$ formulation in the inner region of wall boundary layers and switches to a transformed $K-\epsilon$ formulation in the outer region of boundary layers and in free shear layer/mixing regions. The Chien $K-\epsilon$ model is available in WIND and the SST model is available in both CFL3D and WIND.

Significant work in recent years to implement nonlinear EASM formulations in the CFL3D code has resulted in two models which are currently available. The first EASM is derived in a $K-\epsilon$ form[11,12] and the second is derived in a $K-\omega$ form.[12] Unlike linear two-equation models, EASM formulations are sensitive to turbulent stress anisotropies and have a direct relation to the full Reynolds stress model. As a result, EASM models have the capability to include more relevant flow physics than the linear models. However, they are also solved using a two-equation approach and as a result are not significantly more computationally expensive than linear two-equation models. The $K-\omega$ EASM formulation available in CFL3D was used in the current study. The $K-\epsilon$ EASM model of Rumsey, et al.[11,12] has recently been installed in WIND, as detailed in Ref. 13, and was also investigated in this study.

During the course of the current nozzle calculations, two coefficients controlling the diffusion terms in the underlying two-equation model of the $K-\omega$ EASM installed in CFL3D were modified. As a result, the principal equations defining this model are provided in the following discussion. The turbulent stress tensor of the EASM (for both $K-\epsilon$ and $K-\omega$) is:

$$\begin{aligned}\tau_{ij} = \tfrac{2}{3}K\delta_{ij} - 2\nu_t^*\{S_{ij} - \tfrac{1}{3}S_{kk}\delta_{ij} + \\ [a_2 a_4 \left(S_{ik}W_{kj} - W_{ik}S_{kj}\right) \\ -2a_3 a_4 \left(S_{ik}S_{kj} - \tfrac{1}{3}S_{kl}S_{lk}\delta_{ij}\right)]\}\end{aligned} \tag{1}$$

where S_{ij} is:

$$S_{ij} = \frac{1}{2}\left(\frac{\partial u_i}{\partial x_j} + \frac{\partial u_j}{\partial x_i}\right) \tag{2}$$

and W_{ij} is:

$$W_{ij} = \frac{1}{2}\left(\frac{\partial u_i}{\partial x_j} - \frac{\partial u_j}{\partial x_i}\right) \tag{3}$$

The kinematic eddy viscosity, ν_t^* is:

$$\nu_t^* = C_\mu^* K\tau = -K\alpha_1 \tag{4}$$

where the turbulent time scale is $\tau = 1/\omega = K/\epsilon$. The quantity α_1/τ is equivalent to $-C_\mu^*$ and is obtained from the solution to a cubic equation at every point in the flow field. The solution procedure is described in detail in Ref. 12.

The form of the $K-\omega$ model used in CFL3D as the underlying two-equation model for the EASM is:

$$\frac{DK}{Dt} = \mathcal{P} - f_{\beta^*}K\omega + \frac{\partial}{\partial x_k}\left[\left(\nu + \frac{\nu_t^*}{\sigma_K}\right)\frac{\partial K}{\partial x_k}\right] \tag{5}$$

$$\frac{D\omega}{Dt} = \gamma\frac{\omega}{K}\mathcal{P} - \beta\omega^2 + \frac{\partial}{\partial x_k}\left[\left(\nu + \frac{\nu_t^*}{\sigma_\omega}\right)\frac{\partial\omega}{\partial x_k}\right] \quad (6)$$

where the production of K is given by:

$$\mathcal{P} = -\tau_{ij}\frac{\partial u_i}{\partial x_j} \approx 2\nu_t^* S_{ij}S_{ij} \quad (7)$$

The form of the function f_{β^*} is given in Ref. 12. The two coefficients in the $K-\omega$ EASM that were modified are σ_K and γ. In the original model, $\sigma_K = 2$ and $\gamma = 0.575$. The modified coefficients are $\sigma_K = 1$ and $\gamma = 0.53$. The motivation for this change was that in the original model, the dissipation was too low near boundary layer and shear layer edges, which frequently resulted in abrupt slope changes in predicted mean-flow quantities. The problem was particularly evident for jet flows. In addition, the rate of jet mixing was found to be too low relative to experimental measurements. Reducing σ_K improved results near the edge of the jet considerably. It also improved the slope characteristics near the edge of boundary layers. In Ref. 14, a similar change to σ_K in a linear $K-\epsilon$ model (σ_K changed from 1.36 to 1.0) also resulted in greater mixing and better agreement with experimental observations.

In an effort to maintain the same quality of solutions for a variety of other aerodynamic flowfields of interest, the γ coefficient was simultaneously reduced in the $K-\omega$ EASM considered here. This coefficient multiplies the production term in the ω equation, and it also affects the value of σ_ω, through the equation:

$$\sigma_\omega = \kappa^2/[\sqrt{c_\mu}(\beta-\gamma)] \quad (8)$$

where $\kappa = 0.41$, $\beta = 0.83$, and $c_\mu = 0.0895$.

Use of equation (8) insures correct log-layer characteristics. In the original model, $\gamma = 0.575$ results in $\sigma_\omega = 2.2035$. In the revised model, $\gamma = 0.53$ corresponds to $\sigma_\omega = 1.8730$. Reducing γ also had a beneficial effect for the jet flow case in that the centerline velocity, which was too large using the original model, was reduced to be in better agreement with experimental data.

Overall, changing the two coefficients in the $K-\omega$ EASM model had no significant negative impact when validated for benchmark aerodynamic flows of interest and the change dramatically improved the model's behavior for jet flows. The original and new sets of coefficients are compared in the current study for the Mach 0.94 nozzle case, as will be addressed in the results section.

Computational Grid and Boundary Condition

A computational grid having approximately 2.57 million points distributed across six zones was constructed as follows. Due to horizontal and vertical symmetry of the nozzle configuration shown in Fig. 1, one quadrant of the nozzle was modeled, which is sufficient using the RANS approaches considered here. Examining Fig. 1, the $x-y$ plane of symmetry will be referred to as the major axis, while the $x-z$ plane of symmetry is the minor axis. Figure 2 provides a perspective view of the grid along these two symmetry planes. The nozzle geometry representing the internal flow region upstream of the nozzle exit plane shown in Fig. 1 was represented by 3 zones with point to point match between zones. The grid was packed to the nozzle wall surfaces such that the average y+ of the first point off any wall did not exceed 2.5.

The inflow boundaries of the three zones representing the internal nozzle geometry specified the nozzle stagnation pressure that corresponds to the ideally expanded Mach number of the two cases investigated in this study: $p_T/p_\infty = 1.0644$ for Mach number 0.30 and $p_T/p_\infty = 1.7675$ for Mach number 0.94. The stagnation temperature was set to the ambient static temperature, because the experiments of Zaman and Wang used unheated laboratory air in the nozzle supply lines. Two grid zones were used to represent the ambient air surrounding the nozzle configuration upstream of the nozzle exit plane. The inflows of these two blocks set the inflow stagnation temperature and pressures equal to the ambient static values such that a quiescent ambient condition could be modeled, as existed in the experiment. The three nozzle zones and two ambient inflow zones interfaced with one downstream zone in which the exiting jet flow mixed with the ambient air. The downstream static pressure was set to the ambient pressure.

Turbulence Intensity Calculation

Mean axial velocities and turbulence intensities from the solutions are compared with the experimental data of Zaman and Wang. The axial turbulence intensities were obtained from $\tau_{11} = \overline{u'u'}$ and employing the appropriate turbulent stress expression for each model as follows. From the EASM solutions, the turbulent stress tensor given by equation (1) was used. For the linear one-equation and two-equation model solutions, the Boussinesq approximation was employed:

$$\tau_{ij} = \tfrac{2}{3}K\delta_{ij} - 2\nu_t\left(S_{ij} - \tfrac{1}{3}S_{kk}\delta_{ij}\right) \quad (9)$$

While the two-equation models directly provide the turbulent kinetic energy K used in equation (9), this quantity must be approximated for the one-equation Spalart-Allmaras model. In Ref. 7, this approximation for K is given by:

$$K = \nu_t\sqrt{2S_{ij}S_{ij}}/2a_1 \quad (10)$$

where $a_1 = 0.155$ is the structure parameter.

Results

In this section, results for the Mach 0.30 case, for which there is more extensive experimental data available, are presented first, followed by the Mach 0.94 case results. For each of these two cases, comparisons of CFL3D and WIND results are made within each class of turbulence model, i.e. linear one-equation, linear two-equation, and EASM to isolate any differences from one code to the other when using a similar turbulence model. Then, to highlight differences due to turbulence model, separate results from CFL3D and WIND are presented, for all of the turbulence models used for each code.

Mach 0.30 Nozzle Flow

In order to determine if the computational grid was sufficient for modeling the dominant flow characteristics of the nozzle flows under consideration, a comparison of intermediate solutions obtained with every other point in each computational direction (termed half grid in the subsequent discussion) was made with solutions obtained using the full grid. Figure 3 provides a comparison of axial velocity and turbulence intensity profiles along the major axis obtained from CFL3D calculations with the SST model using the half grid and full grid. While a complete grid sensitivity study would investigate a third computational grid with even more points than that in the current full grid (2.57 million points), the results shown in Fig. 3, with only minor differences between the two solutions, indicate that the full grid is very likely sufficient. Comparisons of solutions for the other turbulence models obtained with the two grids indicated similar agreement as those shown here for the SST results.

A comparison of centerline axial velocities obtained within each class of turbulence model are presented in Fig. 4. For the two models that were used with both CFL3D and WIND (SA and SST), very similar predictions of axial velocity decay were obtained. It may be observed that the SA results indicate closer agreement with the experimental data than the SST or Chien $K-\epsilon$ results. The minor differences in solutions between the Chien $K-\epsilon$ model and SST model (which effectively uses a $K-\epsilon$ model in the jet development region) are most likely due to slight differences in the ϵ equation diffusion coefficient, σ_ϵ, used by the two models.

When attempting EASM calculations with both codes, only the $K-\omega$ EASM (using the new coefficients) resulted in a stable calculation, and even this calculation contained a large scale unsteadiness in the initial part of the jet development region which did not converge to a completely steady flowfield solution. It is believed that the EASM calculations were unable to provide a converged solution for two reasons. First, the nearly incompressible Mach 0.30 nozzle flow exiting into quiescent air naturally leads to slow convergence for solvers such as CFL3D and WIND, which are designed for compressible flow simulations. The second, and likely more important reason is that in examining Fig. 1, it may be observed that there is a very large base region (shown by the cross-hatching) surrounding the lobed nozzle exit, which leads to a highly separated flow, characterized by inherently large scale unsteadiness surrounding the initial jet. The EASM formulations, unlike the linear one-equation or two-equation models, are sensitive to flow anisotropies caused by the large scale unsteadiness present in the initial jet development region considered here. As a result, a time-accurate solution may be warranted for this case, and will be attempted in future efforts. However, from the steady-state calculations attempted here, three intermediate "unsteady" solutions (see Fig. 4(c)), separated by 2000 iterations each, are used to provide an indication of qualitative features of the jet development when using the new $K-\omega$ EASM in CFL3D. Although there is some variability due to the unsteadiness, the essential global features do not change significantly. Therefore, it is believed that an averaged time-accurate computation would exhibit similar results to those shown here. Preliminary time-accurate results on a half grid, not shown here, support this conjecture.

Comparisons of centerline turbulence intensities are provided in Fig. 5. Once again, solutions obtained with the SA and SST models are very similar when using CFL3D and WIND. The experimental data indicate two peaks of turbulence intensity. As indicated in Ref. 3, the first peak occurs when the shear layers from the lobes merge, while the second peak occurs after the outer shear layers merge onto the jet centerline. It may be observed that none of the solutions obtained with the linear one-equation or two-equation models are able to capture the first peak. However, the EASM solutions do indicate the presence of the first peak.

Comparisons of centerline velocities that highlight the effect of the turbulence models in CFL3D and WIND are shown in Figs. 6a and b, respectively. (Only a single representative $K-\omega$ EASM solution is shown for clarity.) Parallel comparisons of centerline turbulence intensities are shown in Figs. 7a and b. In both codes, Fig. 6 indicates that the SA model provides the most rapid mixing and associated jet decay rate. Figure 7 shows substantial variations in the calculated centerline turbulence intensities, with only the $K-\omega$ EASM calculation providing close agreement to the experimental data.

While the centerline profiles shown in Figs. 4 through 7 provide overall indications of the jet decay behavior, more details of the jet decay characteristics along the major and minor axes are shown for the mean axial velocities in Figs. 8 and 9. Detailed turbulence intensity profiles are shown in Figs. 10 and

11. In Fig. 8, it is observed that the SA calculation in both codes indicates the most rapid mixing of the individual lobe shear layers. The velocity profiles along the minor axis also show the most rapid mixing with the SA model, which is also in accordance with the previous centerline comparisons.

The turbulence intensity profiles show substantial variations depending on the turbulence model employed. Interestingly, at the two most downstream measurement stations, $x/D = 12.0$ and $x/D = 18.0$ in Figs. 10 and 11, the SA solution provides the worst agreement with the experimental data. This is due to the fact that the SA model does not directly solve for the turbulent kinetic energy, unlike the other models employed in this study, and the derived turbulent kinetic energy is a function of the strain rate tensor as calculated by equation (10). The result of the SA approximation is that as the velocity profile becomes relatively flat, the calculated turbulence intensity becomes too small. In considering only the mean axial velocity predictions, it may be concluded that the SA model performed as well as any of the models investigated here. However, the deficiency in the SA model farfield turbulence intensity would be undesirable if calculation of the turbulence intensity field is important, as in the case of a jet noise calculation employing the results of RANS flowfield computations.[15,16]

Mach 0.94 Nozzle Flow

As mentioned in the introduction, limitations in using the hot-wire apparatus for extensive use in the high speed flow of the Mach 0.94 case resulted in only centerline quantities being measured. Further, Ref. 3 indicates that the quantitative accuracy of the Mach 0.94 data is questionable. The hot-wire measurements are approximations of mass flux ρu rather than velocity u alone, as described more completely in Refs. 3 and 17. For the Mach 0.30 case, the density is nearly constant throughout the flowfield. While the Mach 0.94 case is not a highly compressible flow, the experimental quantities appearing in the subsequent mean velocity and turbulence intensity plots are actually $\overline{(\rho u)}/\overline{(\rho u)}_{jet}$ and $(\rho u)'_{rms}/\overline{(\rho u)}_{jet}$, respectively.

Comparisons of centerline axial velocities obtained within each class of turbulence model are presented in Fig. 12. Centerline turbulence intensities are provided in Fig. 13. As was the case for the Mach 0.30 results, the CFL3D and WIND implementations of the same models (SA and SST) produced very similar predictions. It may be observed that the SA results indicate closer agreement with the experimental data for the centerline velocities than the SST or Chien $K-\epsilon$ results. Unlike the Mach 0.30 results, the EASM results for Mach 0.94 displayed very little unsteadiness (about an order of magnitude less oscillation in integrated force quantities with CFL3D), yielding essentially converged steady-state solutions in both CFL3D and WIND. However, significantly more iterations were required to obtain solutions with the EASM approaches than with the linear models.

Two $K-\omega$ EASM solutions were obtained, the first using the original settings for σ_K and γ and the second using the new settings. As shown in Fig. 12(c), the $K-\omega$ EASM solution using the new coefficients provided the highest level of mixing and closest agreement with experimental data. In Fig. 13, none of the solutions accurately capture the presence of the first turbulence intensity peak, but the $K-\omega$ EASM (new) solution indicates smaller discrepancies in prediction of the initial rise in turbulence intensity than the other two EASM solutions. Interestingly, the CFL3D $K-\omega$ EASM solution with the original coefficient settings and the WIND $K-\epsilon$ EASM solution produce similar results.

The comparisons of centerline velocities using all of the turbulence models in CFL3D and WIND are shown in Figs. 14a and b. Comparisons of centerline turbulence intensities are shown in Figs. 15a and b. As was the case for the Mach 0.30 results, Fig. 14 indicates that the SA model provides the fastest jet decay rate. Figure 15 shows substantial variations in the calculated centerline turbulence intensities, with none of the solutions providing close agreement with the experimental data, although it is emphasized again that the Mach 0.94 experimental data was documented to have substantially more uncertainty than the Mach 0.30 data.

Conclusions

The capabilities of several turbulence models in two general purpose RANS solvers, CFL3D and WIND, were investigated for a highly three-dimensional flowfield originating from a six-lobed nozzle. Two nozzle operating points were considered, corresponding to Mach 0.30 and Mach 0.94 nozzle exit conditions. Linear one-equation and two-equation models and nonlinear $K-\omega$ and $K-\epsilon$ EASM turbulence models were examined. Calculations obtained with the same linear eddy viscosity models installed in the two codes yielded very similar results, while much more substantial differences were noted when varying the type of turbulence model within either single code. This indicates that the effects of turbulence modeling are significantly greater than any differences in code numerics between CFL3D and WIND.

Solutions obtained with the SA one-equation linear turbulence model generally indicated reasonable agreement with experimental data in terms of the mean axial velocity predictions. However, turbulence intensity predictions did not agree well with the experimental data. This is believed to be due to the approximation for turbulent kinetic energy which is required with the SA model in order to derive the turbulent stress components. Calculations with the SST

and Chien $K-\epsilon$ two-equation linear turbulence models resulted in significantly delayed initial mixing rates of the jet with surrounding ambient air, when comparing both the mean axial velocities and turbulence intensities with experimental data. Further downstream, the two-equation models yielded reasonable agreement with the data. None of the linear models were able to reproduce the experimental observation of two distinct turbulence intensity peaks along the jet centerline.

Two new coefficients for σ_K and γ in the $K-\omega$ EASM model were described in the context of the current jet flowfield. Although the changes were originally motivated by poor behavior for jet flow cases, these new coefficients are now also recommended in this model for general use as well. Specifically, for the Mach 0.94 case, results with the new coefficients resulted in improved mixing over results using the original coefficients. The $K-\epsilon$ EASM yielded delayed mixing similar to $K-\omega$ EASM results using the original coefficients.

For the Mach 0.30 case, the $K-\epsilon$ EASM was unable to run in a stable manner. The $K-\omega$ EASM ran successfully, but the calculation exhibited unsteady behavior and did not converge completely to a steady state solution. This behavior was believed to be primarily due to natural unsteadiness in the flowfield just downstream of the nozzle exit with large base region. The unsteadiness of the $K-\omega$ EASM solution indicates the need to properly simulate this flow with a time-accurate calculation. The better convergence characteristics of the linear models is probably not an indication of higher accuracy of these simpler models, but instead that they are able to more effectively smear the unsteadiness in the initial jet development region with their less sophisticated isotropic eddy viscosity formulations. In fact, an examination of three unsteady intermediate flowfields produced by the $K-\omega$ EASM indicated that only this model was able to reproduce the two peaks of centerline turbulence intensity that was observed in the experiment.

Future efforts will include obtaining a $K-\omega$ EASM calculation in a time-accurate mode in order to more accurately simulate the complex initial jet development region. Since the new $K-\omega$ EASM settings for σ_K and γ indicate promise for flow problems dominated by turbulent mixing such as the nozzle flow considered here, further investigations of these and other coefficients should be conducted for jet and similar mixing-dominated flows. Previous to this work, most calibrations of the coefficients in the underlying two-equation models have been performed for wall-bounded turbulent flows.

Acknowledgements

This work was sponsored by the Propulsion and Power Program at NASA Glenn Research Center. Mr. David W. Lam and Ms. Mary Jo Long-Davis were project managers for this work.

References

[1]Barber, T.J., Chiappetta, L.M., DeBonis, J.R., Georgiadis, N.J., and Yoder, D.A., "An Assessment of Parameters Influencing the Prediction of Shear Layer Mixing," *Journal of Propulsion and Power*, Vol. 15, No. 1, 1999, pp. 45-53.

[2]Georgiadis, N.J., Yoder, D.A., and DeBonis, J.R., "A Comparison of Three Navier-Stokes Solvers for Exhaust Nozzle Flowfields," AIAA Paper 99-0748, Jan. 1999.

[3]Zaman, K.B.M.Q. and Wang, F.Y., "Noise, Turbulence, and Thrust of Subsonic Free Jets from Lobed Nozzles," AIAA Paper 2002-0569, Jan. 2002.

[4]Nelson, C.C. and Power, G.D., "CHSSI Project CFD-7: The NPARC Alliance Flow Simulation System," AIAA Paper 2001-0594, Jan. 2001.

[5]Krist, S.L., Bierdon, R.T., and Rumsey, C.L., "CFL3D User's Manual (Version 5.0)," NASA TM-1998-208444, June 1998.

[6]Spalart, P.R., and Allmaras, S.R., "A One-Equation Turbulence Model for Aerodynamic Flows," *La Recherche Aerospatiale*, No. 1, 1994, 1994, pp. 5-21.

[7]Spalart, P.R., and Allmaras, S.R., "A One-Equation Turbulence Model for Aerodynamic Flows," AIAA Paper 92-0439, Jan. 1992.

[8]Chien, K.-Y., "Predictions of Channel and Boundary Layer Flows with a Low-Reynolds-Number Turbulence Model," *AIAA Journal*, Vol. 20, No. 1, 1982, pp. 33-38.

[9]Menter, F. R., "Two-Equation Eddy-Viscosity Turbulence Models for Engineering Applications," *AIAA Journal*, Vol. 32, No. 8, 1994, pp. 1598-1605.

[10]Menter, F.R., "Zonal Two Equation k - ω Turbulence Models for Aerodynamic Flows," AIAA Paper 93-2906, July 1993.

[11]Rumsey, C.L., Gatski, T.B., and Morrison, J.H., "Turbulence Model Predictions of Strongly Curved Flow in a U-Duct," *AIAA Journal*, Vol. 38, No. 8, 2000, pp. 1394-1402.

[12]Rumsey, C.L. and Gatski, T.B., "Recent Turbulence Model Advances Applied to Multielement Airfoil Computations," *Journal of Aircraft*, Vol. 38, No. 5, 2001, pp. 904-910.

[13]Yoder, D.A., "Initial Evaluation of an Algebraic Reynolds Stress Model for Compressible Turbulent Shear Flows," AIAA Paper 2003-0548, Jan. 2003.

[14]Georgiadis, N.J., Chitsomboon, T., and Zhu, J., "Modification of the Two-Equation Turbulence Model in NPARC to a Chien Low Reynolds Number $k-\epsilon$ Formulation ," NASA TM 106710, Sept. 1994.

[15]Khavaran, A. and Georgiadis, N.J., "Aeroacoustics of Supersonic Elliptic Jets ," AIAA Paper 96-0641, Jan. 1996.

[16]Khavaran, A., "Role of Anisotropy in Turbulent Mixing Noise," *AIAA Journal*, Vol. 37, No. 7, 1999, pp. 832-841.

[17]Zaman, K.B.M.Q. and Tam, C.K.W., "Flow and Noise Field of Subsonic Jets from Asymmetric Nozzles," AIAA Paper 99-3583, June 1999.

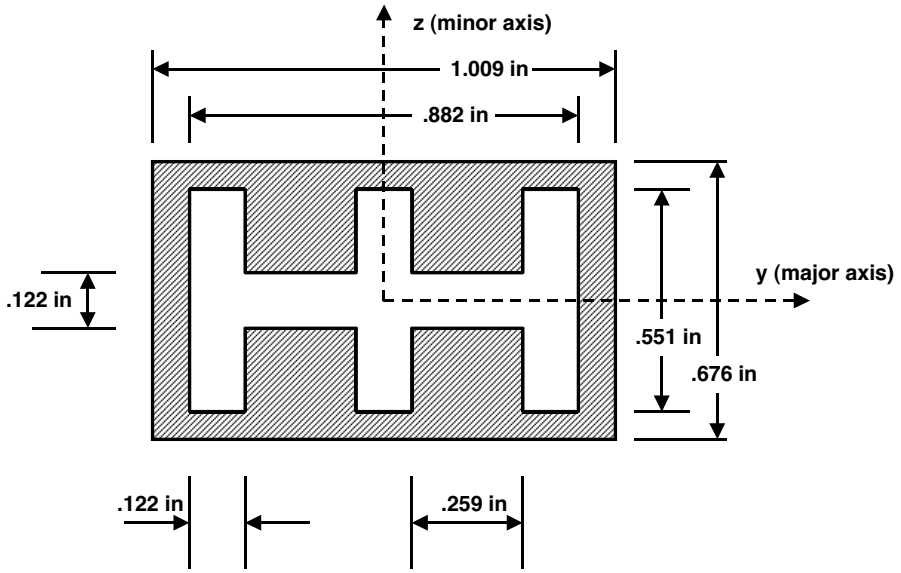

Fig. 1 Schematic of nozzle exit for six-lobed configuration.

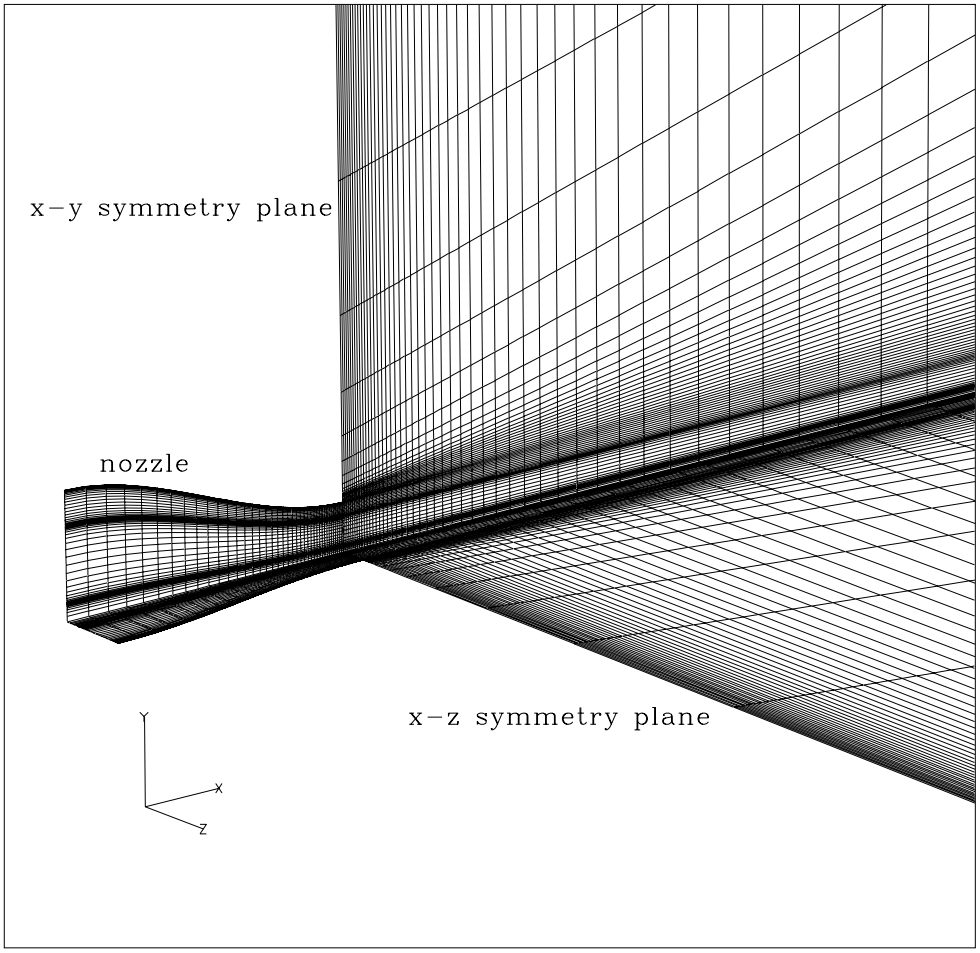

Fig. 2 Perspective view of grid along symmetry planes (every other point shown for clarity).

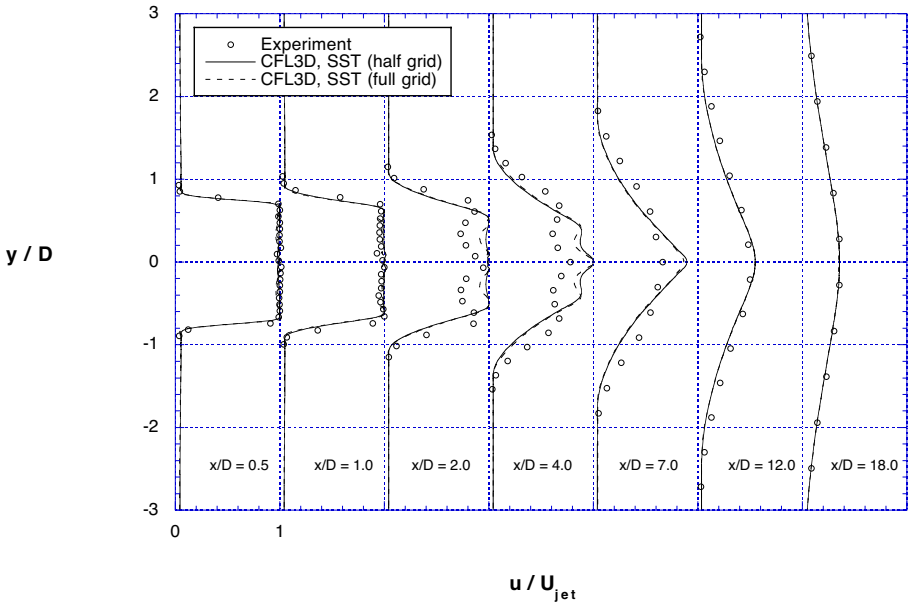

a) Mean velocities along major axis

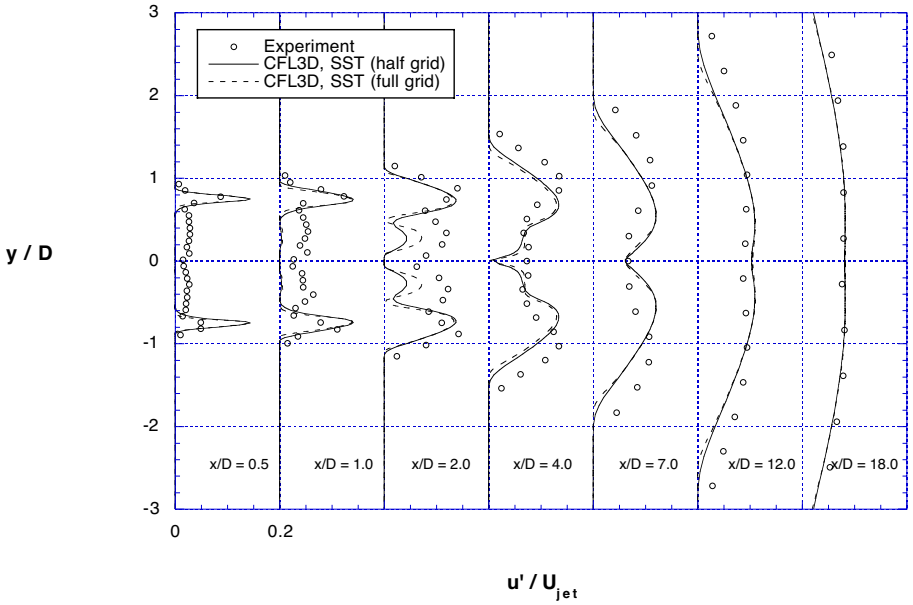

b) Turbulence intensities along major axis

Fig. 3 Grid sensitivity effects using CFL3D, SST turbulence model.

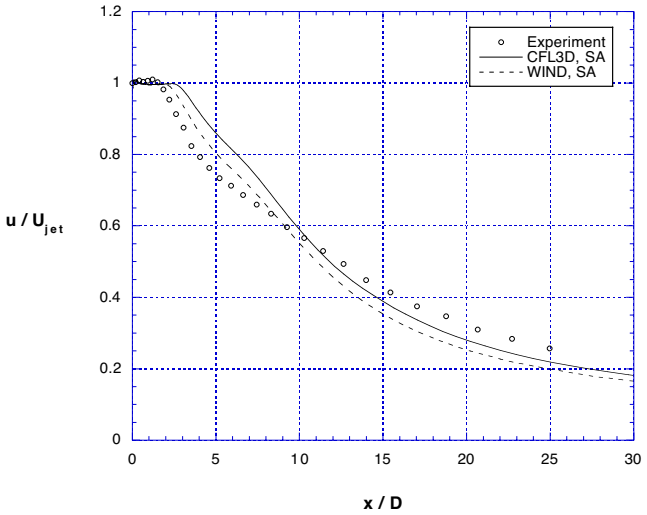

a) One-equation models

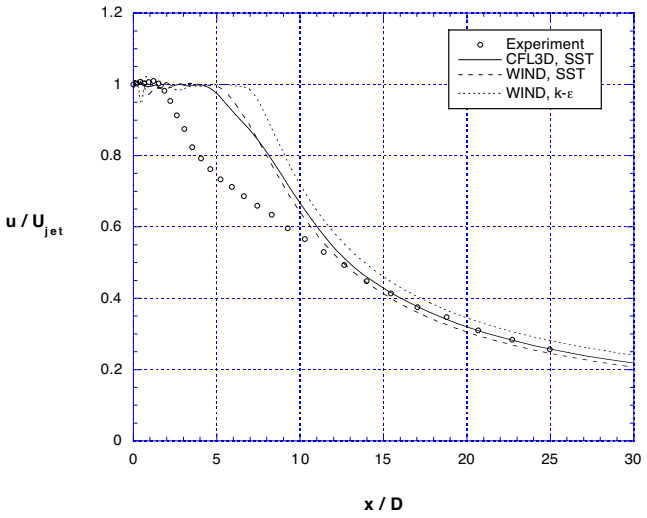

b) Two-equation models

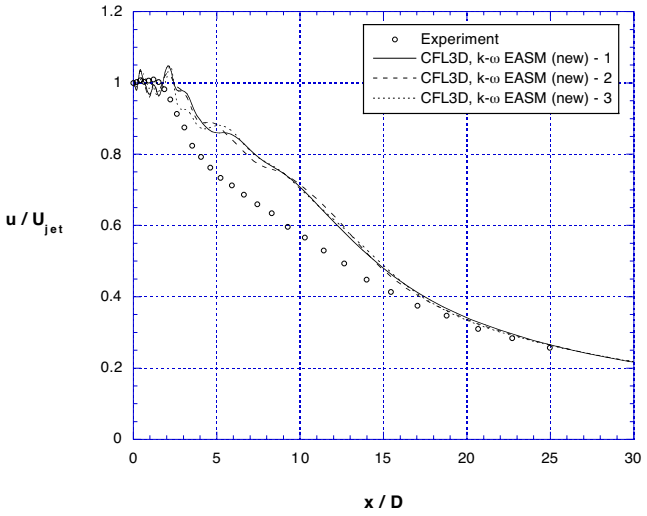

c) Explicit algebraic stress models

Fig. 4 Mean velocities along the centerline for the Mach 0.30 case using CFL3D and WIND.

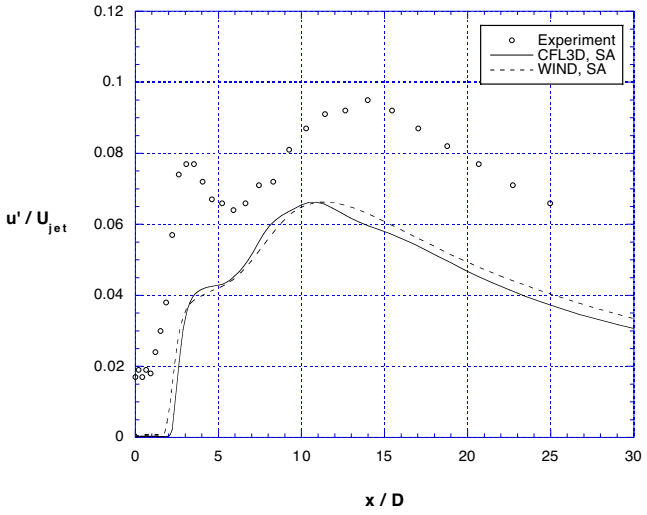

a) One-equation models

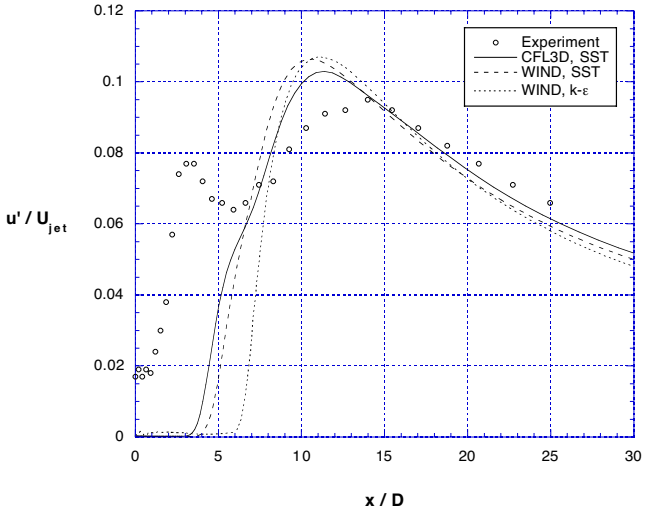

b) Two-equation models

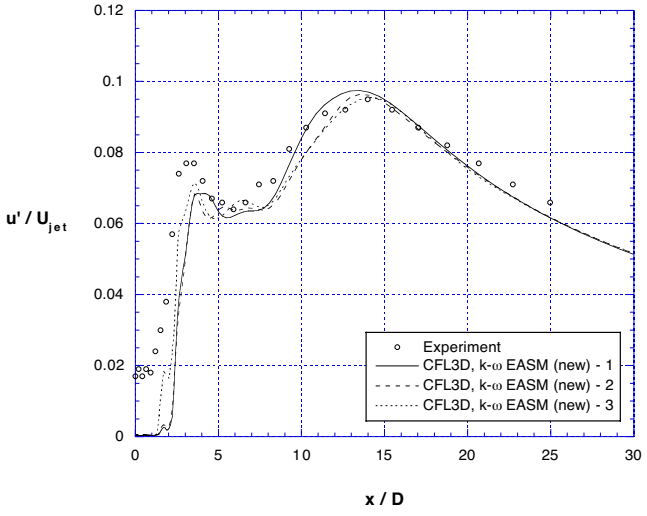

c) Explicit algebraic stress models

Fig. 5 Turbulence intensities along the centerline for the Mach 0.30 case using CFL3D and WIND.

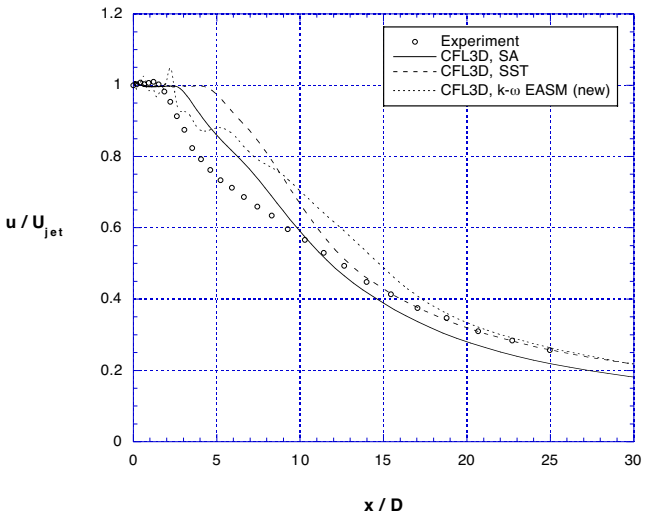

a) CFL3D

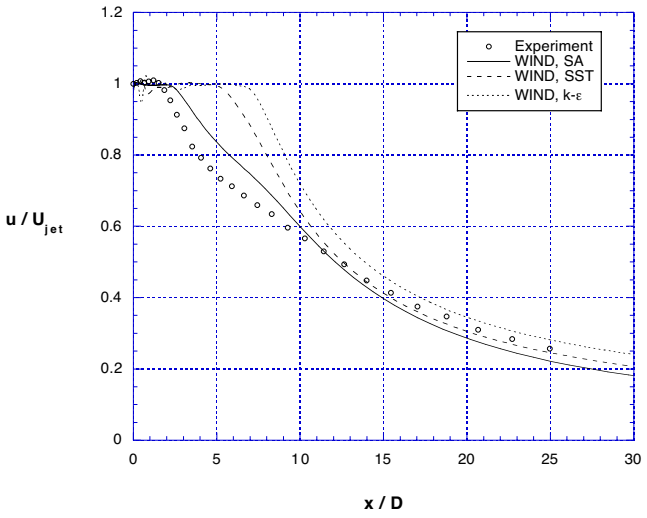

b) WIND

Fig. 6 Turbulence model effects on mean velocities along the centerline for the Mach 0.30 case.

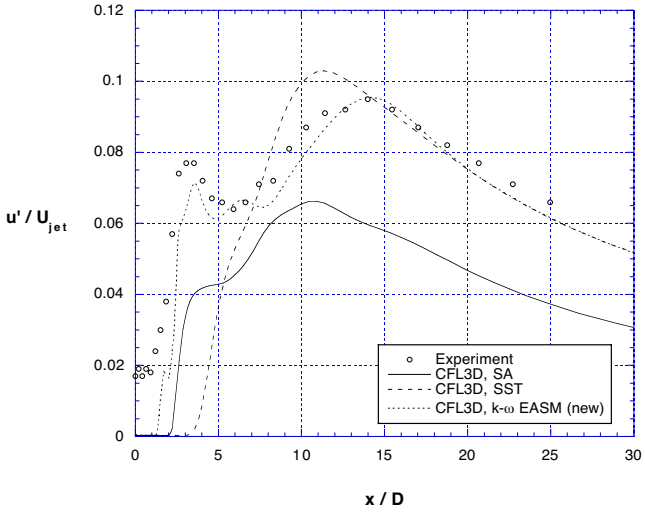

a) CFL3D

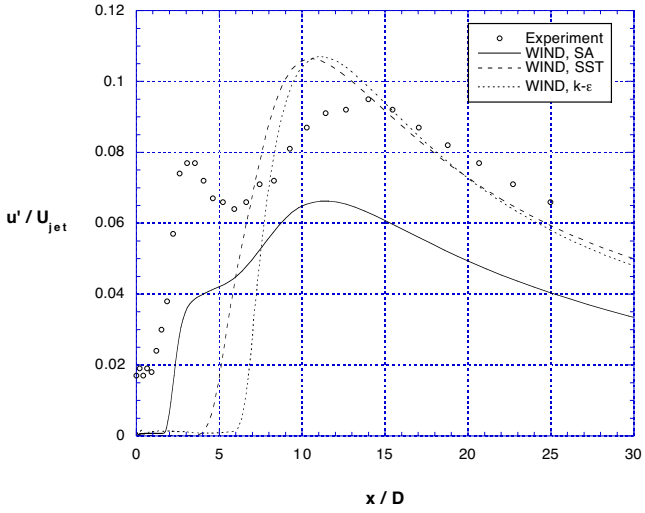

b) WIND

Fig. 7 Turbulence model effects on turbulence intensities along the centerline for the Mach 0.30 case.

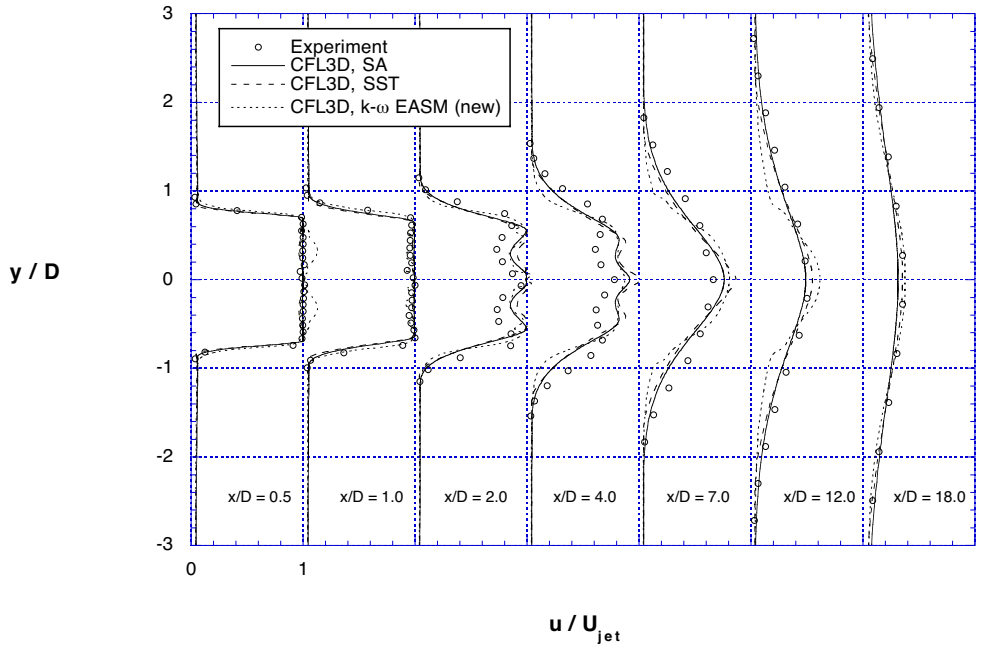

a) CFL3D

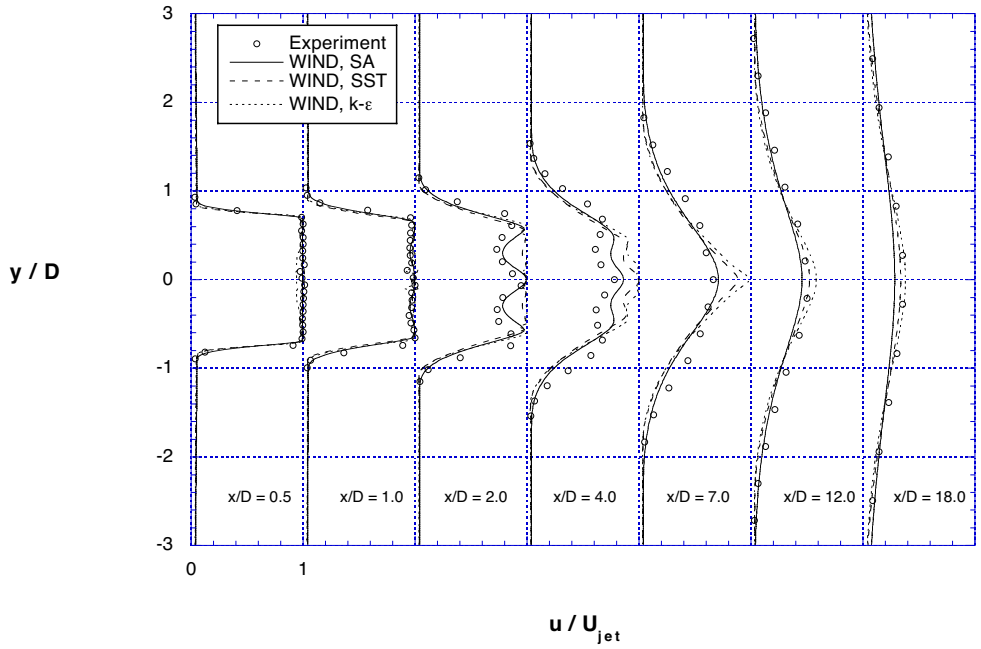

b) WIND

Fig. 8 Turbulence model effects on mean velocity profiles along the major axis for the Mach 0.30 case.

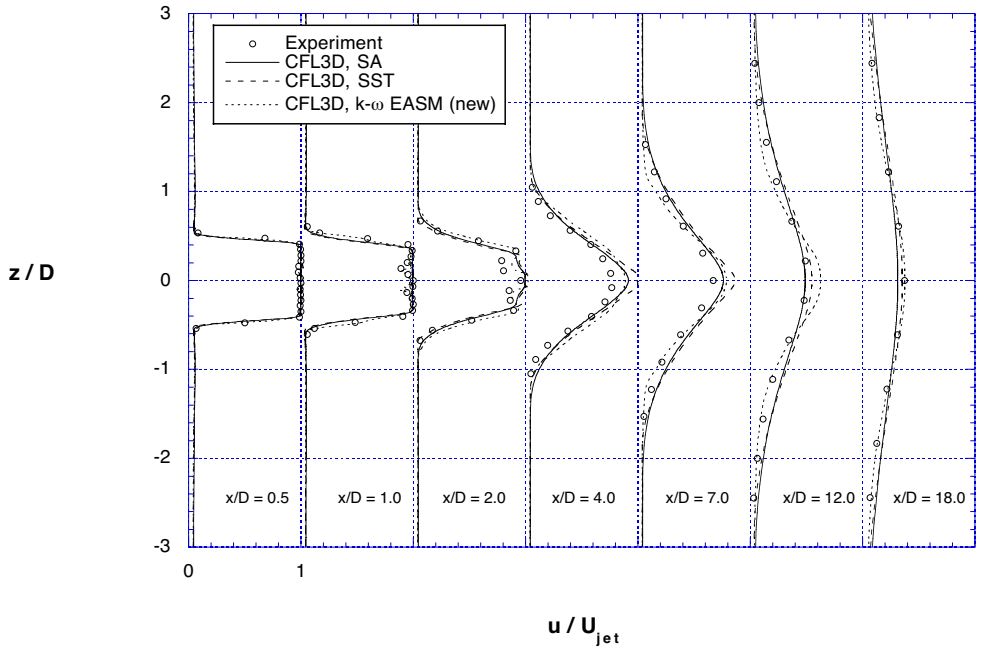

a) CFL3D

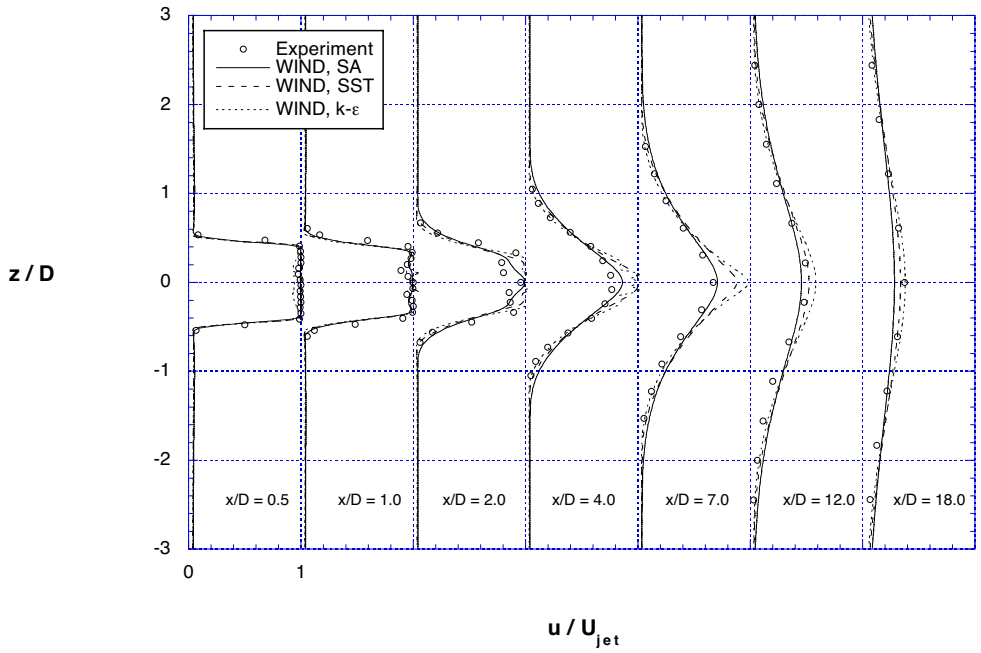

b) WIND

Fig. 9 Turbulence model effects on mean velocity profiles along the minor axis for the Mach 0.30 case.

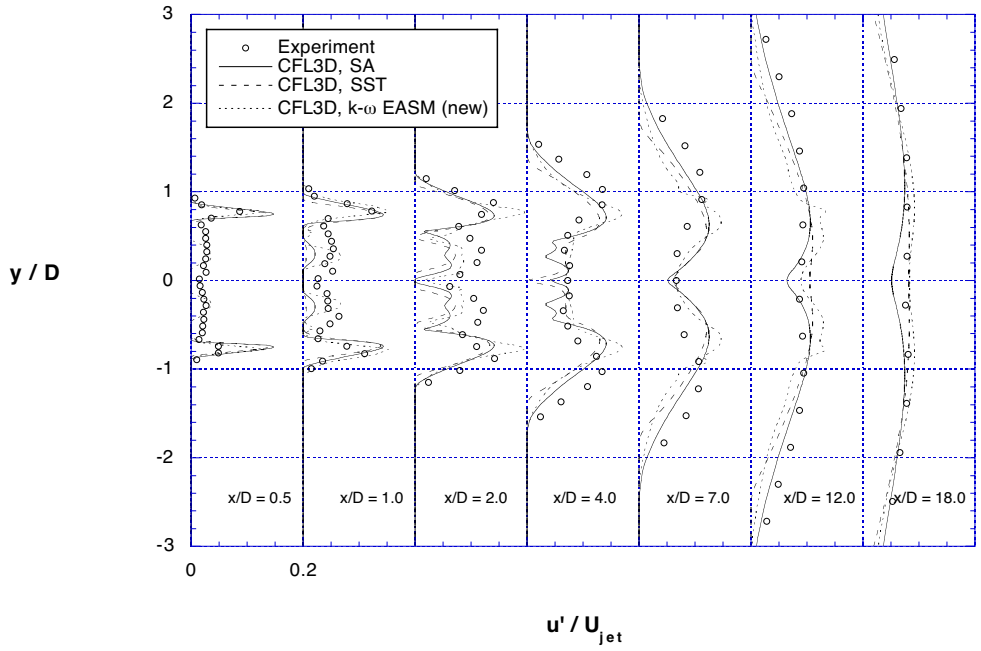

a) CFL3D

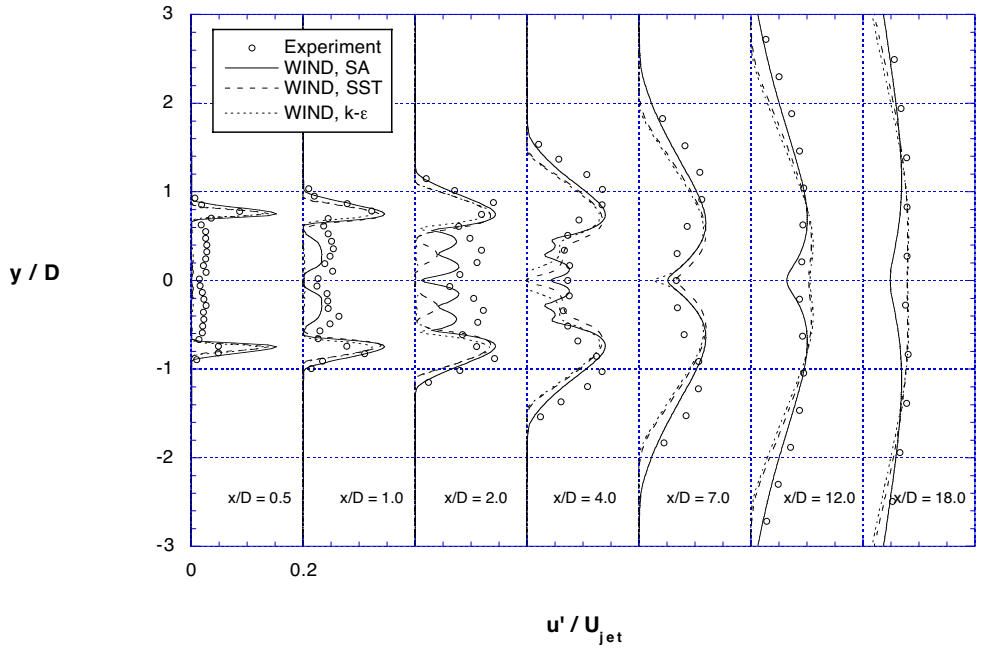

b) WIND

Fig. 10 Turbulence model effects on turbulence intensity profiles along the major axis for the Mach 0.30 case.

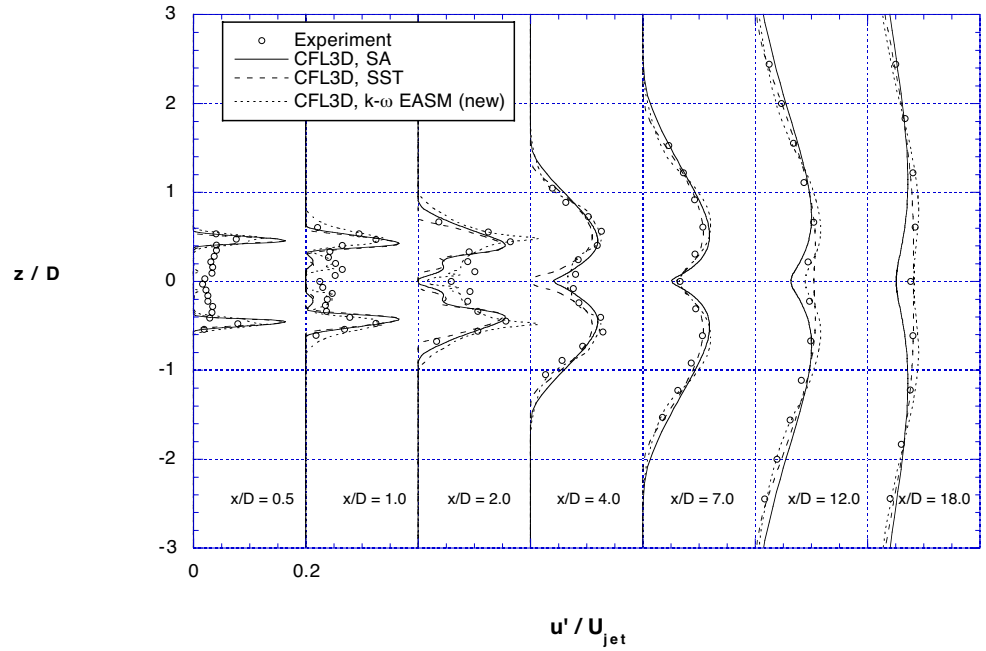

a) CFL3D

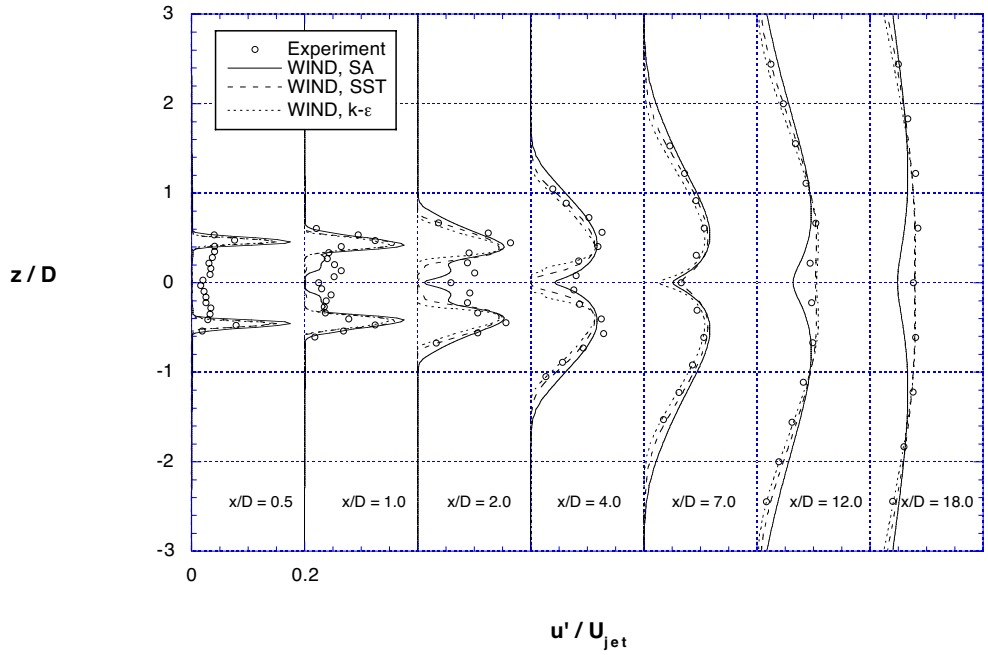

b) WIND

Fig. 11 Turbulence model effects on turbulence intensity profiles along the minor axis for the Mach 0.30 case.

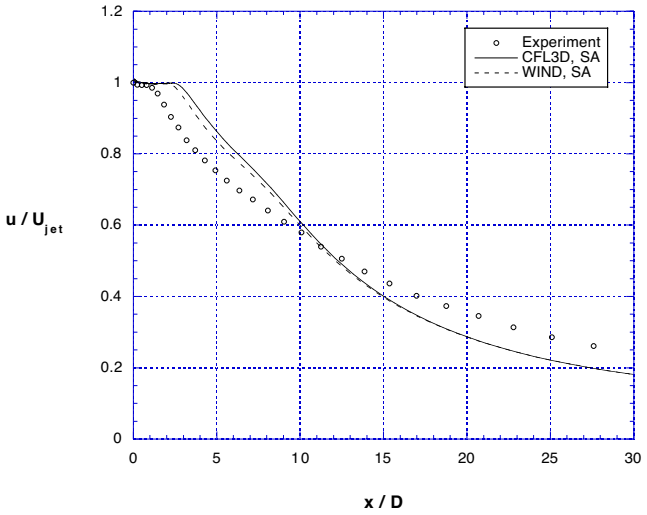

a) One-equation models

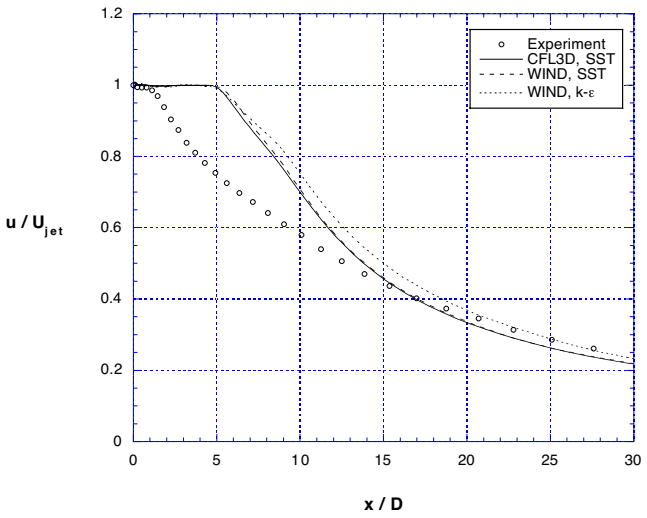

b) Two-equation models

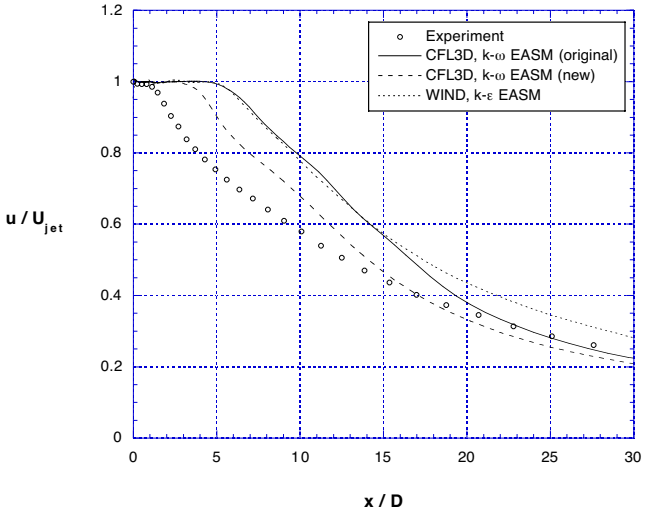

c) Explicit algebraic stress models

Fig. 12 Mean velocities along the centerline for the Mach 0.94 case using CFL3D and WIND.

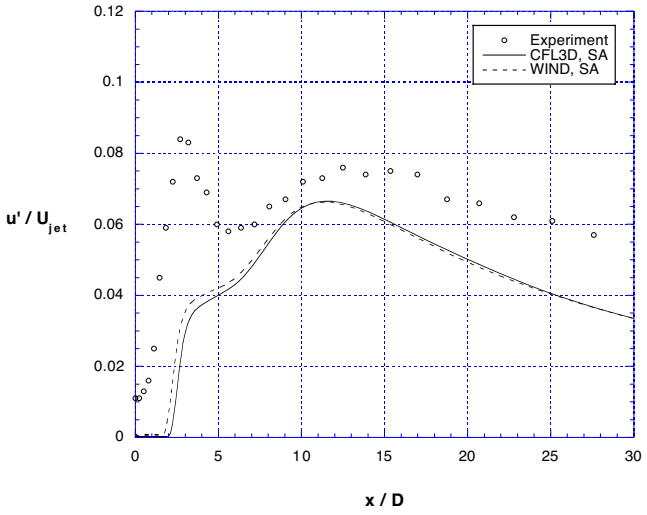

a) One-equation models

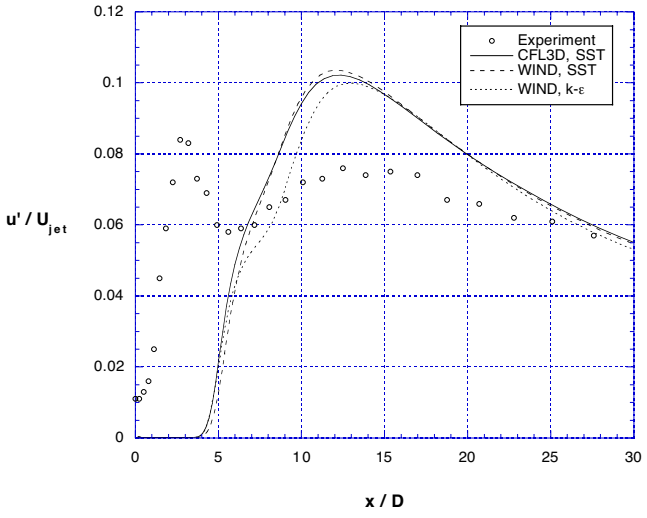

b) Two-equation models

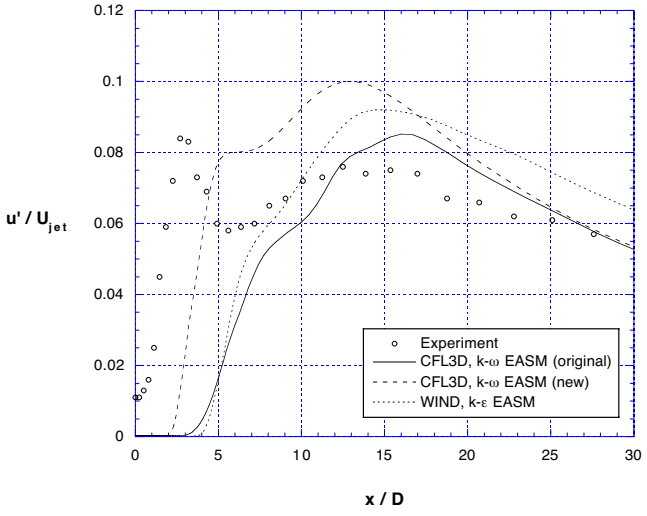

c) Explicit algebraic stress models

Fig. 13 Turbulence intensities along the centerline for the Mach 0.94 case using CFL3D and WIND.

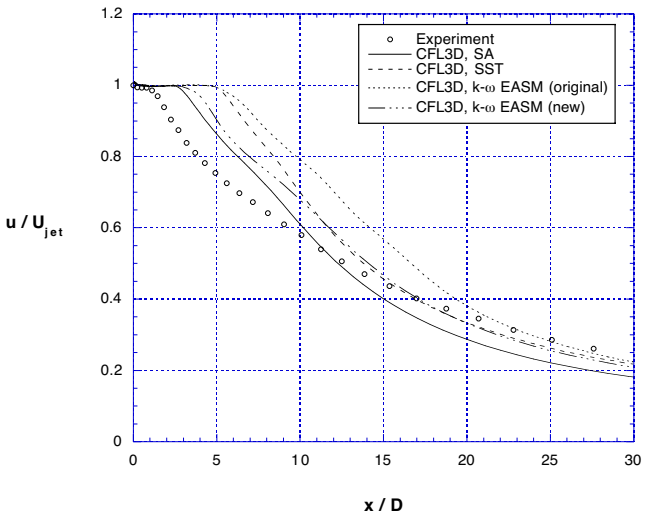

a) CFL3D

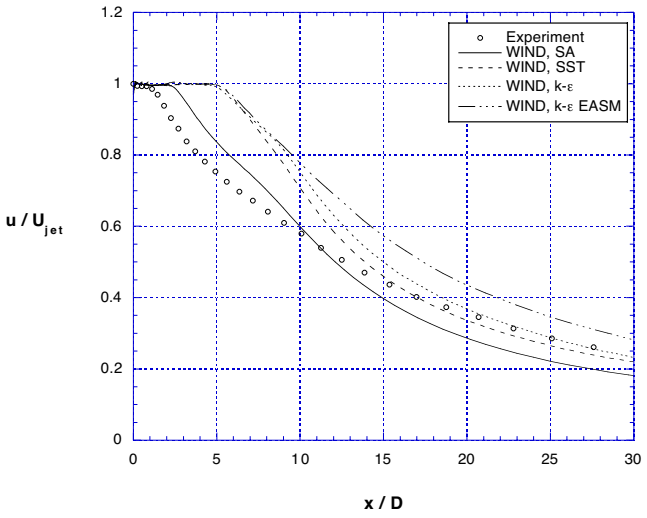

b) WIND

Fig. 14 Turbulence model effects on mean velocities along the centerline for the Mach 0.94 case.

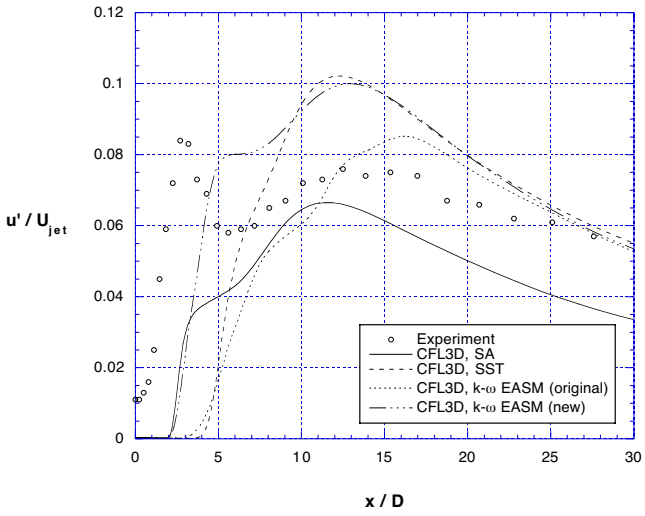

a) CFL3D

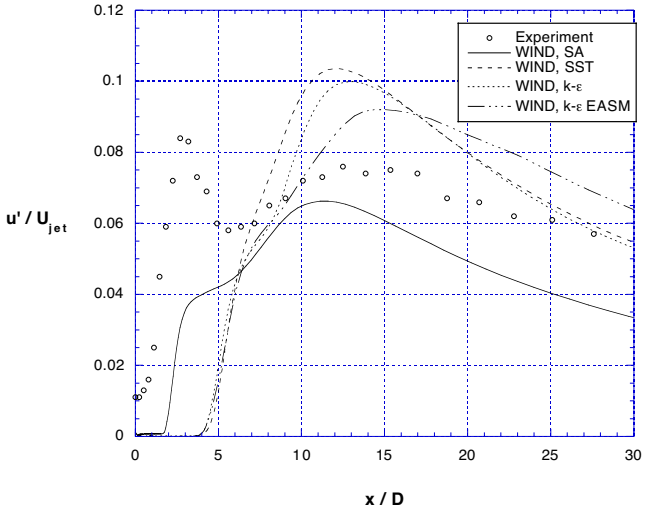

b) WIND

Fig. 15 Turbulence model effects on turbulence intensities along the centerline for the Mach 0.94 case.